

Detent-Force Minimization of Double-Sided Interior Permanent-Magnet Flat Linear Brushless Motor

Young-Shin Kwon and Won-jong Kim

Department of Mechanical Engineering, Texas A&M University, College Station, TX 77843-3123 USA

New detent-force minimization methodologies for a 6/4 double-sided interior permanent-magnet flat linear brushless motor configured with alternate teeth windings are presented in this paper. Based on the superposition principle, the end-effect and cogging forces are separately minimized using two different techniques. The end-effect force is reduced by a new 2-D optimization using the step-shaped end frames in the slotless stators. The cogging force is minimized through a destructive interference using the slot-phase shift between the upper and lower stators. Each technique is verified experimentally, and the optimal design parameters are formulated using Fourier series. The total detent-force reduction of 94% is achieved as compared with the base model. The steady-state force after applying these new detent-force-free techniques is demonstrated with actual measurements, and also compared with the finite-element analysis result and analytic solution.

Index Terms—Cogging force, detent force, end-effect force, interior permanent-magnet flat linear brushless motor (IPM-FLBM).

I. INTRODUCTION

SINCE THE advent of practical linear motors in the 1970s, they have been extensively used in biomedical equipment, semiconductor fabrication, machine-tool sliding tables, and factory automation. They became an indispensable component in linear motion-control systems. Especially, the linear brushless motor (LBM) is the most popular one due to its numerous advantages, such as fewer space harmonics, fewer end turns, higher energy efficiency, and simpler control. LBMs can be classified into the slotted iron-core and air-core types according to stator configurations. The slotted iron-core LBM can be constructed with the surface-mounted permanent magnet (SPM) or interior permanent magnet (IPM) [1]. This can also be constructed by the single-sided or double-sided structures. Especially, since the double-sided structure can produce much larger force in a given volume, it is appropriate in high-force density applications [1]. However, its large detent force due to the end-effect and cogging forces is a significant drawback in high-precision motion control at low speed. Since the end-effect force is caused by the stator's finite length, it does not exist in a rotary motor. This end-effect force can also be a major or minor detent force depending on the configuration of the number of slots and poles with respect to its cogging force. Furthermore, it is not easy to formulate these detent forces with high nonlinearity with a generalized analytic solution.

Due to the advancement of the numerical analysis based on finite-element analysis (FEA) tools, however, various detent-force-minimization techniques, such as skewed PM placement [2], semiclosed slots [2], [3], stator having auxiliary teeth [3], [4], overall length extension of stator [5], alternative

fractional slot-pole structure [6], and asymmetric PM placement [7], [8], were developed previously. Although these techniques reduced the detent forces effectively, some methods increased fabrication difficulties, such as oversized magnet, elaborated winding process, postoptimization for additional teeth, excessively lengthy stator, and variously sized iron-cores [1]–[8]. Recently, a PM pole-shift method useful for mass production was introduced for a double-sided SPM linear motor [9], but this technique cannot be applied to an IPM linear motor.

Thus, this paper presents new detent-force minimization techniques for the double-sided 6/4 IPM-FLBM having two short-length stators configured with alternate teeth windings. The end-effect and cogging forces are separately investigated to minimize the total detent force by two independent techniques with the superposition principle. The end-effect force is reduced by a 2-D optimization using an analytic solution and verified by experimental measurements for the slotless stator with an adjustable length and various stack widths. The net cogging force is minimized by a destructive interference technique using the slot-phase shift between the upper and lower stators. The optimal slot-phase shift is determined by an analytic solution using Fourier series and also verified with 3-D-FEA and measurements. The optimal slot-phase-shift model is merged with the optimized slotless model. Finally, the steady-state thrust force and the minimized effective detent force according to mover positions are measured, and compared with the 3-D-FEA result and analytic solution.

II. BASE MODEL ANALYSIS

A. Double-Sided 6/4 IPM-FLBM Structure

An advantage of linear motors compared with their rotary counterparts is that a double-sided configuration is possible. Since this configuration can produce a much larger thrust force than the single-sided type in a given volume, it is suitable for the applications that require high thrust forces. In general, the IPM types can produce a greater air-gap flux density by the flux-focusing effect and an additional reluctance force than the

Manuscript received June 26, 2015; revised August 26, 2015; accepted October 28, 2015. Date of publication November 3, 2015; date of current version March 16, 2016. Corresponding author: W.-J. Kim (e-mail: wjkim@tamu.edu).

Color versions of one or more of the figures in this paper are available online at <http://ieeexplore.ieee.org>.

Digital Object Identifier 10.1109/TMAG.2015.2497298

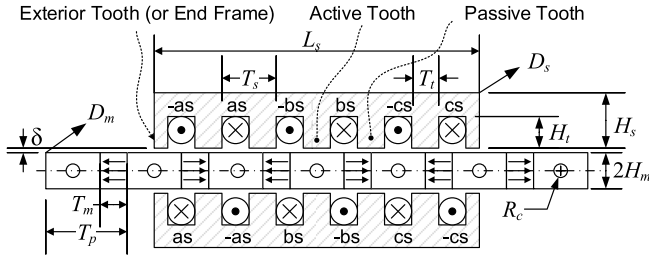


Fig. 1. Base model of the double-sided 6/4 IPM-FLBM with alternate teeth windings.

TABLE I
MECHANICAL DESIGN SPECIFICATIONS OF THE BASE MODEL

Parameters	Symbols	Values (m)
Air gap	δ	0.001
Stack width of stator	D_s	0.020
Stack width of mover	D_m	0.020
Stator height	H_s	0.011
Stator tooth height	H_t	0.007
One half off PM height	H_m	0.004
PM width	T_m	0.006
Pole pitch	T_p	0.018
Slot pitch	T_s	0.012
Tooth width	T_t	0.006
Overall stator length	L_s	0.072
Mover core mount hole	R_c	0.003

* SS400 is used for soft-iron core material, and NdFeB 45 for PM.

SPM types. Fig. 1 shows the base model for the 6/4 double-sided IPM-FLBM with alternate teeth windings on the basis of the stator of a rotary brushless dc motor [10], [11]. Therefore, the passive tooth between phases *a* and *c* in a rotary motor is substituted with two exterior teeth at both ends of the stator in order to accomplish the fully balanced flux paths for the six-step current control [12]. As a result, three active and four passive teeth are configured. The specifications of this base model are listed in Table I.

B. Steady-State Thrust and Detent Forces

Since the end-effect force occurs at end frames or exterior teeth regardless of the stator length, the end-effect force of a linear motor with a short stator length takes a relatively larger portion of the total thrust force than that with a long stator [6]. It has a period of the pole pitch. On the other hand, the cogging force acting on one slot also has the same period, but the total cogging force of a linear motor with a fractional-slot configuration does not have the first-harmonic force owing to the destructive interference between the cogging forces of each slot. In this perspective, the detent force of the base model shown in Fig. 2 implies that since it is mainly governed by the first-harmonic force term with respect to the pole pitch, the end-effect force is the major detent force in the base model. This FEA also shows that the thrust force in the low-current mode (200 A-turns) is distorted proportionally by the detent force, but the thrust force in the high-current mode (1000 A-turns) is affected differently by the detent force depending on the specific position of the mover. This is

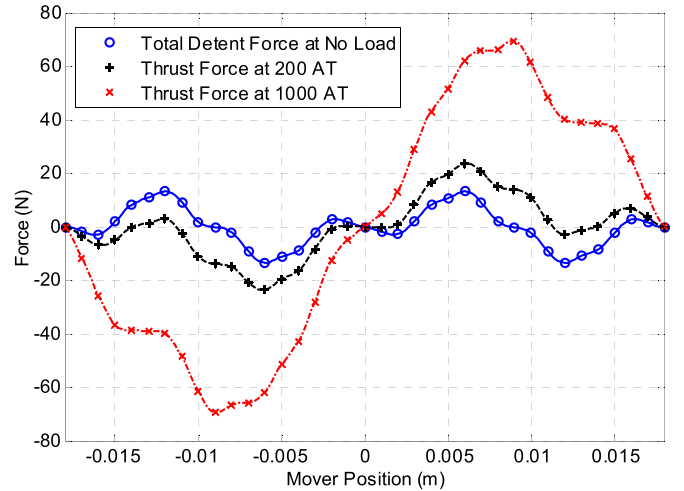


Fig. 2. FEA results for the thrust and detent forces of the base model according to the mover positions.

because the magnetic flux density of the iron-core material is saturated due to the high current. These results indicate that the total effective thrust force cannot be estimated through the summation of the detent force and the expected sinusoidal thrust force and that the detent force should be minimized in order to produce the undistorted thrust force according to the mover positions.

III. DETENT-FORCE MINIMIZATION

In this section, assuming that the total detent force can be expressed as the linear superposition of the end-effect and cogging forces, the minimization techniques for each force are investigated separately. In the end, the combined effective detent force is evaluated.

A. 1-D End-Effect-Force Minimization

As mentioned in Section II-B, since the end-effect force is the major detent force in the base model, the minimization of the end-effect force is the most effective way to reduce the total detent force. Since the end-effect force is governed only by the finite distance between the two end frames in the stator, the end-effect force can be minimized by the stator's overall length adjustment [5], [13]. According to [13], the cogging force of a single rectangular-prism iron-core structure can be expressed in Fourier series with the period of the pole pitch. The end-effect forces for the left and right ends, and the total resultant force of a single rectangular-prism iron-core structure can be given, respectively, by

$$F_L = a_0 + \sum_{n=1}^{\infty} a_n \cos\left(\frac{2\pi n}{T_p}\left(x - \frac{L_s}{2}\right)\right) + \sum_{n=1}^{\infty} b_n \sin\left(\frac{2\pi n}{T_p}\left(x - \frac{L_s}{2}\right)\right) \quad (1)$$

$$F_R = -F_L(-(x+L_s)) = -a_0 - \sum_{n=1}^{\infty} a_n \cos\left(\frac{2\pi n}{T_p}\left(x + \frac{L_s}{2}\right)\right) + \sum_{n=1}^{\infty} b_n \sin\left(\frac{2\pi n}{T_p}\left(x + \frac{L_s}{2}\right)\right) \quad (2)$$

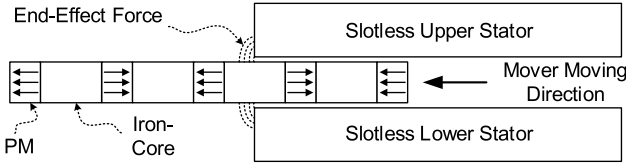


Fig. 3. Left end-effect force measurement using the slotless rectangular-prism iron-core stator when the mover's position is at zero.

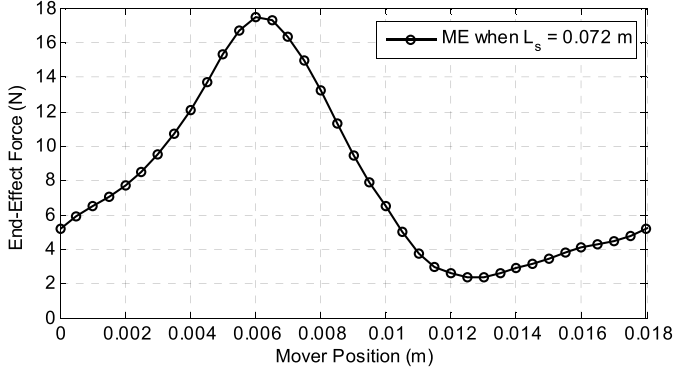


Fig. 4. Measured left end-effect force according to mover positions when the pole pitch is 0.018 m, and the magnet length is 0.006 m.

$$F_E = F_L + F_R = 2 \sum_{n=1}^{\infty} \left[a_n \sin \left(\frac{\pi n L_s}{T_p} \right) + b_n \cos \left(\frac{\pi n L_s}{T_p} \right) \right] \times \sin \left(\frac{2\pi n}{T_p} x \right) \quad (3)$$

where F_L is the left end-effect force, F_R is the right end-effect force, F_E is the total end-effect force, and a_n and b_n are the Fourier coefficients. The total end-effect force (3) indicates that it can be minimized if the overall length of the stator has the following relationship:

$$a_n \sin \left(\frac{\pi n L_s}{T_p} \right) + b_n \cos \left(\frac{\pi n L_s}{T_p} \right) = 0 \Rightarrow L_s = 2PT_p - \frac{T_p}{n\pi} \tan^{-1} \left(\frac{b_n}{a_n} \right) \quad (4)$$

where P is the number of pole pairs of the mover. Hence, if the Fourier coefficients in (1) can be determined from the left end-effect force experimentally, the specific harmonic term of the end-effect force can be removed through the stator's length adjustment. In order to verify this method, the left end-effect force of the slotless iron-core stator shown in Fig. 3 was measured experimentally instead of using the FEA because there is a difference between the mechanical and magnetic lengths [5]. The measured end-effect force in Fig. 4 describes that the end-effect force has the maximum value at 0.006 m. The period of 0.018 m is the same as the pole pitch (T_p).

Table II shows the Fourier coefficients of (1) calculated by curve-fitting from the measurement given in Fig. 4. These coefficients show that the first-harmonic force is dominant. Thus, if applying (4) in order to remove the first-harmonic force, the optimal overall stator length can be chosen as 0.0788 m with $n = 1$ and $P = 2$. The experimental results in Fig. 5 show that the end-effect forces vary according to the slotless

TABLE II
ESTIMATED FOURIER COEFFICIENTS OF THE LEFT END-EFFECT FORCE

Harmonic order (n)	a_n	b_n
0	7.943	0.000
1	-2.441	5.924
2	0.387	-2.311
3	0.449	0.275
4	-0.167	0.267
5	-0.059	-0.095
6	-0.002	0.052
7	-0.065	0.027

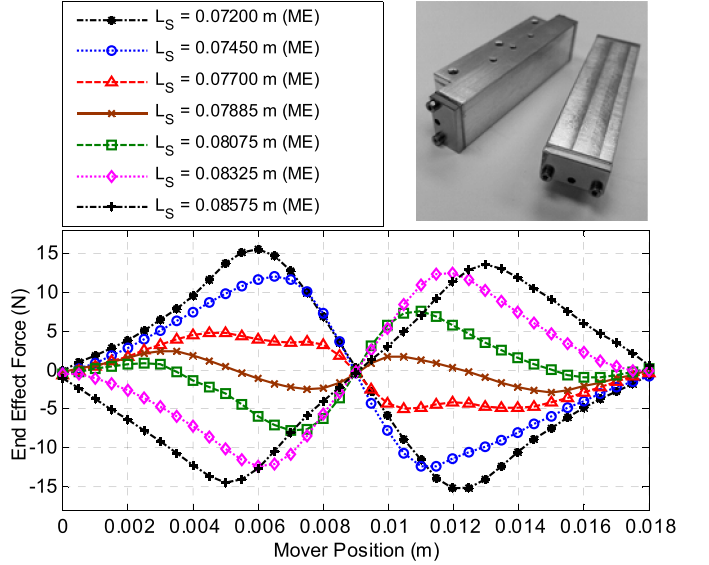


Fig. 5. Measured end-effect forces according to the slotless stator's overall lengths and mover positions.

stator's overall lengths and the mover positions. The maximum end-effect force of over 15 N is generated in the base model. The end-effect force analysis in Fig. 6(a) and (b) describes that the optimal overall length is 0.0788 m to minimize the end-effect force. This result is in good agreement with the optimal overall length estimated by (4) for the first-harmonic force. This also shows that the conventional approach using a half-pitch extension of the stator is not optimal although it can reduce the end-effect force to some extent.

B. 2-D End-Effect-Force Minimization

The end-effect force was reduced by 83% through the 1-D overall length optimization as compared with the base model. However, the result in Fig. 6(b) shows that the second-harmonic force still remains because the proposed method can remove only one selected harmonic force according to (4). Thus, in order to further minimize the end-effect force, the second-harmonic force should also be removed. In [5], the smooth-formed edge shape is added at both ends of the stator for the further reduction of the remaining end-effect force. However, since this technique needs the optimal length plus an additional two pole-pitch length in the base model, it is not appropriate for the stator requiring a short length. In this

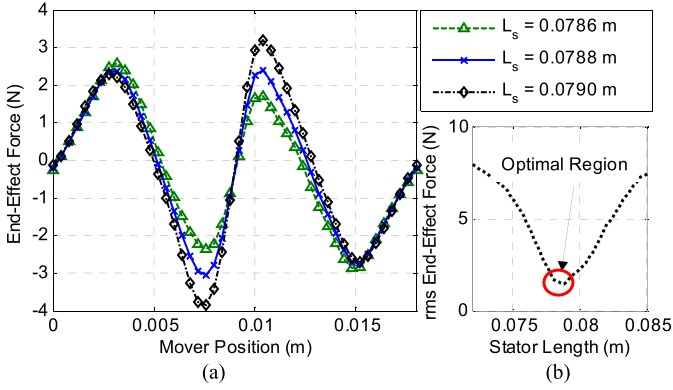


Fig. 6. (a) Optimal stator length analysis according to mover positions with respect to the peak-to-peak end-effect forces. (b) RMS end-effect force according to the stator lengths.

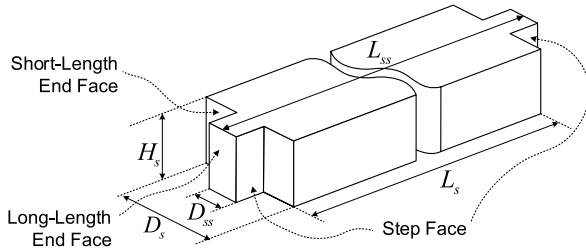


Fig. 7. Dimension definition of the slotless stator with two different lengths.

sense, the experimental results in Fig. 5 show that since the two end-effect forces for the lengths of 0.0745 and 0.0833 m have an opposite phase, the end-effect force can be further reduced without the excessive length extension of the stator if a slotless stator with two different lengths shown in Fig. 7 is employed. Therefore, assuming no lateral force perpendicular to the step faces formed by the two different lengths, and the mechanical stack width (D_{ss}) of the long-length portion is the same as the effective stack width (D_{sse}), the end forces acting on the end faces of the long-length portion and the short-length portion can be expressed as (5) and (6) from (3), respectively

$$F_{LSS} = 2 \frac{D_{sse}}{D_s} \sum_{n=1}^{\infty} \left[a_n \sin \left(\frac{\pi n L_{ss}}{T_p} \right) + b_n \cos \left(\frac{\pi n L_{ss}}{T_p} \right) \right] \times \sin \left(\frac{2\pi n}{T_p} x \right) \quad (5)$$

$$F_{LS} = 2 \left(\frac{D_s - D_{sse}}{D_s} \right) \sum_{n=1}^{\infty} \left[a_n \sin \left(\frac{\pi n L_s}{T_p} \right) + b_n \cos \left(\frac{\pi n L_s}{T_p} \right) \right] \times \sin \left(\frac{2\pi n}{T_p} x \right) \quad (6)$$

where F_{LSS} and F_{LS} are the end-effect forces of the long- and short-length portions, respectively. L_{ss} is the longer stator length, L_s is the shorter stator length, and D_s is the total stack width of the stator. In (5) and (6), assuming that D_{sse} is a half of D_s , the total end-effect force of the upper and lower stators

with two different lengths can be given as

$$F_E = F_{LSS} + F_{LS} = 2 \sum_{n=1}^{\infty} A_n B_n \sin \left(\frac{2\pi n}{T_p} x \right) \quad (7)$$

where

$$A_n = a_n \sin \left(\frac{\pi n}{2T_p} (L_{SS} + L_S) \right) + b_n \cos \left(\frac{\pi n}{2T_p} (L_{SS} + L_S) \right)$$

$$B_n = \cos \left(\frac{\pi n}{2T_p} (L_{SS} - L_S) \right).$$

The above equation indicates that the total end-effect force can be minimized when either A_n or B_n is zero. From these two conditions, the relations between the two different lengths in a stator and the harmonic order can be given by

$$L_{SS} + L_S = 2(2PT_p) - \frac{2T_p}{n\pi} \tan^{-1} \left(\frac{b_n}{a_n} \right) \quad (8)$$

$$L_{SS} - L_S = \frac{T_p}{n}. \quad (9)$$

The above two equations state that two selected harmonic forces can be removed by two different lengths (L_{SS} and L_S) of a stator, as shown in Fig. 7. Thus, removing the dominant components in the end-effect force is very effective. In this case, (8) and (9) can be used to remove the first- and second-harmonic forces, respectively. The choice of these harmonic orders can also be switched, but the overall stator length would be longer than that from the former choice. Equation (10) shows the two different lengths implemented in a stator when the harmonic orders (n) for (8) and (9) are 1 and 2, respectively, in order to remove the first- and second-harmonic forces

$$\begin{bmatrix} L_{SS} \\ L_S \end{bmatrix} = \begin{bmatrix} 1 & 1 \\ 1 & -1 \end{bmatrix}^{-1} \begin{bmatrix} 2(2PT_p) - (2T_p/\pi) \tan^{-1}(b_1/a_1) \\ T_p/2 \end{bmatrix}. \quad (10)$$

Since such optimal lengths can be established when assuming no lateral force on the four step faces formed between the long and short lengths, the effect for the four step faces should be considered. In order to investigate this effect, the two lengths of 0.0745 and 0.0835 m obtained from Table II and (10) were employed in both the upper and lower stators. And then, the total end-effect forces were measured according to the stack widths of the long-length portion of the stator. As expected, the results in Fig. 8 show that the end-effect force has been increased rather in a half stack width ($D_{ss} = 0.01$ m) for the precondition of (7) as compared with the 1-D optimization. This implies that the effective stack width to satisfy (7) is not the same as the mechanical stack width. This is the same as taking Carter's principle into account when calculating the air-gap permeance in the slotted stator [14].

Therefore, from (5) and (6), and the measured end-effect forces in Fig. 8, the effective stack-width ratio for the mechanical stack-width ratio is investigated, as shown in Fig. 9. The dashed line shows the relationship when there is no lateral force on the step faces. The circles show the values computed through comparisons of the measured results in Fig. 8 and the

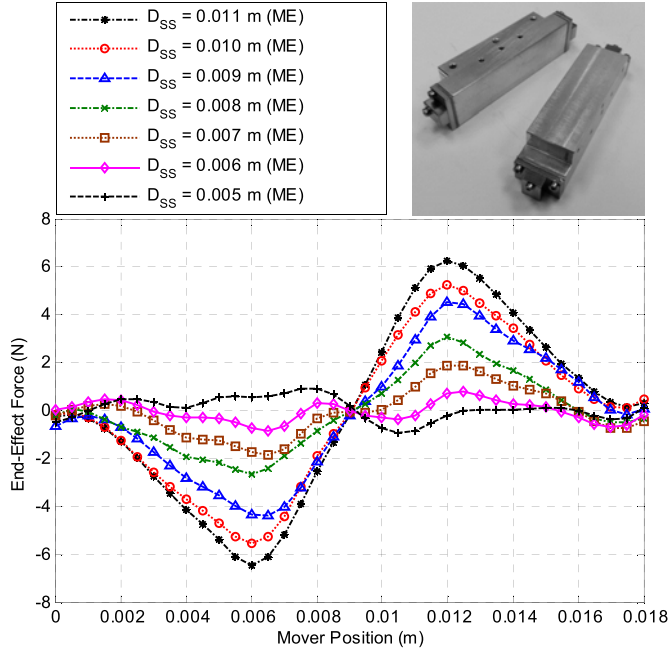


Fig. 8. Measured end-effect forces according to the mover positions with respect to the stack widths of the long-length portion.

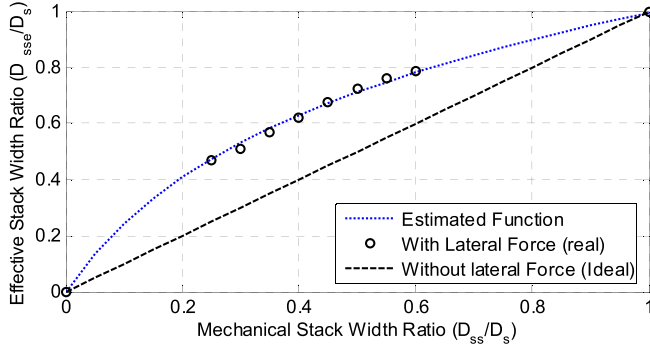


Fig. 9. Effective stack-width ratio according to the mechanical stack-width ratio of the long-length portion in the stator when $L_{ss} - L_s = 0.009$ m and $\delta = 0.001$ m.

sum of (5) and (6) for the corresponding stack width. The dotted line describes a conversion function fitting the circled data and given as

$$\frac{D_{sse}}{D_s} = \frac{1}{2} \ln \left(1 + 2\pi \frac{D_{ss}}{D_s} \right). \quad (11)$$

Thus, applying the conversion function (11) to (5) and (6), they can be rewritten as

$$F_{LSS} = \ln \left(1 + 2\pi \frac{D_{ss}}{D_s} \right) \sum_{n=1}^{\infty} C_n \sin \left(\frac{2\pi n}{T_p} x \right) \quad (12)$$

$$F_{LS} = \left(2 - \ln \left(1 + 2\pi \frac{D_{ss}}{D_s} \right) \right) \sum_{n=1}^{\infty} D_n \sin \left(\frac{2\pi n}{T_p} x \right) \quad (13)$$

where

$$C_n = a_n \sin \left(\frac{\pi n L_{ss}}{T_p} \right) + b_n \cos \left(\frac{\pi n L_{ss}}{T_p} \right)$$

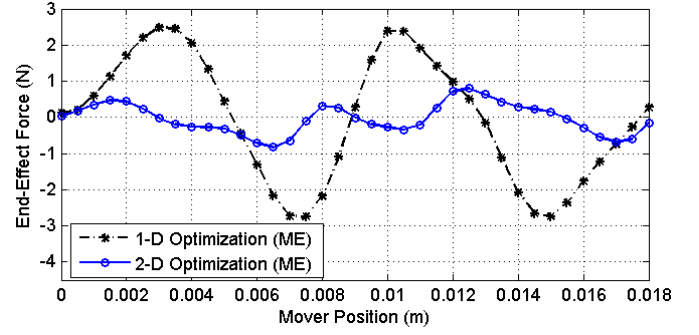


Fig. 10. End-effect force comparison of the 1-D optimization ($L_s = 0.0788$) and 2-D optimization ($L_{ss} = 0.0835$ m, $L_s = 0.0745$ m, $D_s = 0.02$ m, and $D_{ss} = 0.006$ m).

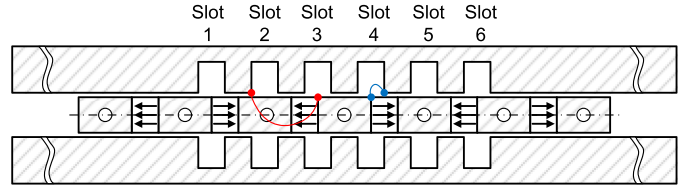


Fig. 11. Infinite-length stator model for the cogging force analysis.

and

$$D_n = a_n \sin \left(\frac{\pi n L_s}{T_p} \right) + b_n \cos \left(\frac{\pi n L_s}{T_p} \right).$$

According to the above equations, when the mechanical stack width of the long-length portion is 0.0055 m, the effective stack-width ratio of the long-length and short-length portions is 0.5. Thus, (7) becomes valid, and the end-effect force can be minimized through the two lengths obtained from (10). The empirical conversion function (11) obtained in this paper needs more experiments for other cases in order to be a general formula. However, if (9) is chosen to remove the second-harmonic force as the same manner in (10), since the optimal-length difference between the two lengths has a half of pole pitch in every case, (11) can be used in various pole-pitches of the same inset-type IPM configuration with the air gap of 0.001 m. Fig. 10 shows that the 2-D optimization can reduce the detent force further than that with 1-D optimization. The second-harmonic force that remains in the 1-D optimization was removed in the 2-D optimization. As a result, the end-effect force was reduced by 83% with the 1-D optimization and by 94% with the 2-D optimization, respectively, with respect to the base model.

C. Cogging-Force Minimization

In this section, the cogging force minimization is discussed. Fig. 11 shows the 6-slot stator and 4-pole mover model with an infinite length.

The left edge of each slot has an attractive force with the right edge of the mover core, and the right edge of each slot has an attractive force with the left edge of the mover core. Thus, if the previous end-effect force model in (3) is employed,

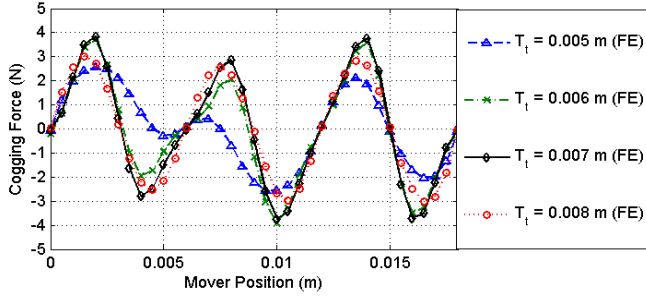


Fig. 12. FEA results for cogging forces of the infinite-length stator model according to the mover positions with respect to the stator's tooth widths.

the cogging force acting on one slot can be given as

$$F_{\text{cog},m} = \sum_{k=1}^{\infty} F_k \sin\left(\frac{2\pi k}{T_p}(x + (m-1)T_s)\right) \quad (14)$$

where m is the slot number, and F_k is the magnitude of the k th-harmonic component. If there is no change in the ratio of the pole and slot pitches, the above relationship is valid although the magnitude of each harmonic component may change depending on the slot width and magnetic saturation condition. Thus, since the total number of slots in the 6/4 configuration is 6, the total cogging force can be expressed as

$$F_{\text{cog}} = \sum_{m=1}^6 \sum_{k=1}^{\infty} F_k \sin\left(\frac{2\pi k}{T_p}(x + (m-1)T_s)\right). \quad (15)$$

Since the 6/4 configuration has the relation ($2T_p = 3T_s$), the cogging forces of the m th and $(m+3)$ th slots are theoretically equal. Thus, (15) can be rewritten as

$$\begin{aligned} F_{\text{cog}} &= 2 \sum_{m=1}^3 \sum_{k=1}^{\infty} F_k \sin\left(\frac{2\pi k}{T_p}(x + (m-1)T_s)\right) \\ &= 2 \sum_{k=1}^{\infty} F_k \left[1 + 2 \cos\left(\frac{2\pi k}{T_p}T_s\right)\right] \sin\left(\frac{2\pi k}{T_p}x\right) \\ &= \begin{cases} 0, & \text{for } k \neq 3n \\ 2 \sum_{k=1}^{\infty} F_k \left[1 + 2 \cos\left(\frac{2\pi k}{T_p}T_s\right)\right] \sin\left(\frac{2\pi k}{T_p}x\right), & \text{for } k = 3n. \end{cases} \end{aligned} \quad (16)$$

The above equation implies that the total cogging force has only triple- n th-harmonic components, whereas the other components cancel each other regardless of the values of F_k even if the magnitude of the triple- n th-harmonic forces becomes twice as larger. The FEA results in Fig. 12 show that the first- and second-harmonic forces are eliminated by the destructive interference of the 6/4 configuration, and the third-harmonic force is dominant regardless of the force-magnitude change by the slot width. This also implies that (16) is valid. Although the first- and second-harmonic cogging forces are cancelled by the destructive interference of each slot, the remaining third-harmonic force is still large for the precision control of a linear motor.

Thus, adopting a semiclosed slot geometry or increasing the least common multiple between the number of stator slots

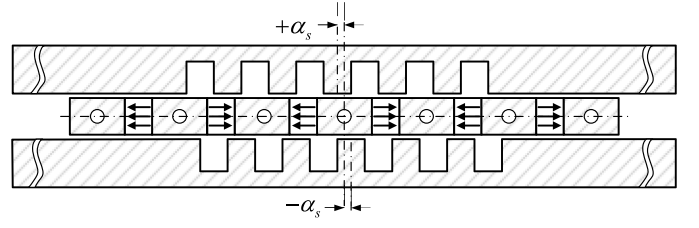


Fig. 13. Concept of the slot-phase shift configuration in the double-sided IPM-FLBM, where α_s is the slot-phase shift.

and the number of rotor poles can be an alternative way to reduce the remaining harmonic forces [3], [6]. However, these methods would complicate the winding fabrication, as well as are inappropriate in compact-sized motors. The asymmetrical PM placement presented in [7] and [8] is ineffective in the IPM configuration because this technique needs variously sized magnets and iron-cores, as well as the previously minimized end-effect force is not applicable. The PM pole-shift technique introduced in [9] is also unavailable in the double-sided IPM configuration. However, if the basic principle for the stepped rotor skew in rotary motors or the PM phase-shift in SPM linear motors is adopted as a form of the slot-phase shift between the upper and lower stators, as shown in Fig. 13, the remaining triple- n th-harmonic cogging forces can be removed without the modification for the fractional slot or winding configuration.

Furthermore, since the lower stator is just the rotation of the upper stator with respect to the lateral axis, only two types of iron-core lamination plates are required. Therefore, this new method has an advantage in manufacturability as well and can be implemented on the double-sided SPM structure, and its performance can be predicted by the analytic solution developed in this section. From this conceptual design, the total cogging force of (16) can be decomposed into the cogging forces of the upper and lower stators as

$$\begin{aligned} F_{\text{cog}} &= \underbrace{\sum_{k=1}^{\infty} F_k \left[1 + 2 \cos\left(\frac{2\pi k}{T_p}T_s\right)\right] \sin\left(\frac{2\pi k}{T_p}(x - \alpha_s)\right)}_{\text{Cogging Force of Upper Stator}} \\ &\quad + \underbrace{\sum_{k=1}^{\infty} F_k \left[1 + 2 \cos\left(\frac{2\pi k}{T_p}T_s\right)\right] \sin\left(\frac{2\pi k}{T_p}(x + \alpha_s)\right)}_{\text{Cogging Force of Lower Stator}} \\ &= 2 \sum_{k=1}^{\infty} F_k \left[1 + 2 \cos\left(\frac{2\pi k}{T_p}T_s\right)\right] \cos\left(\frac{2\pi k \alpha_s}{T_p}\right) \sin\left(\frac{2\pi k}{T_p}x\right). \end{aligned} \quad (17)$$

Eventually, when the design parameter α_s is $T_p/12$, and $2T_p = 3T_s$, the total cogging force has only the sixth-harmonic force as (18) regardless of F_k

$$F_{\text{cog}} = \begin{cases} 0, & \text{for } k \neq 6n \\ 2 \sum_{k=1}^{\infty} F_k \left[1 + 2 \cos\left(\frac{4\pi k}{3}\right)\right] \cos\left(\frac{\pi k}{6}\right) \sin\left(\frac{2\pi k}{T_p}x\right), & \text{for } k = 6n. \end{cases} \quad (18)$$

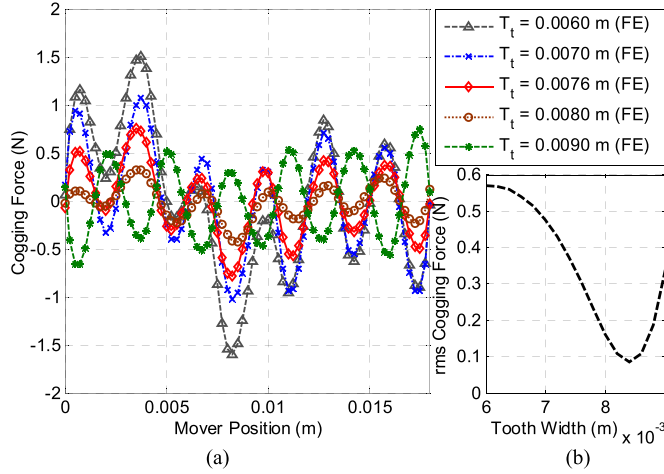


Fig. 14. FEA results for the stator with the slot-phase shift of $T_p/6$ between the upper and lower stators. (a) Total cogging forces and (b) RMS cogging force according to the tooth widths.

TABLE III
FINAL DESIGN PARAMETERS OF STATOR

Parameters	Symbols	Values (m)
Stator's stack width of short-length portion	D_s	0.0200
Stator's stack width of long-length portion	D_{ss}	0.0060
Tooth width	T_t	0.0076
Shorter length of stator	L_s	0.0745
Longer length of stator	L_{ss}	0.0835
Slot-phase shift	α_s	0.0015

The FEA results in Fig. 14(a) show that the cogging forces have only the sixth-harmonic term when the slot-phase shift of $T_p/12$ is employed in the upper and lower stators, respectively. These results are in good agreement with (18). In addition, these results in Fig. 14 show that the magnitudes of the sixth-harmonic forces are determined by the magnitude of F_k according to slot widths. The rms cogging force in Fig. 14(b) shows that the slot width of 0.0084 m is optimal to minimize the cogging force.

D. Detent-Force-Free Stator

Table III shows the final design parameters implemented on a new stator in the double-sided 6/4 IPM-FLBM. The lengths of the long- and short-length portions in the stator were determined as 0.0835 and 0.0745 m, respectively. The stack width of the long-length portion was determined as 0.0060 m in order to use the available machined pieces although 0.0055 m is the optimal stack width of the long-length portion according to (11). The slot-phase shifts of $+0.0015$ and -0.0015 m were applied in the upper and lower stators with respect to the stator center line. As a result, the total slot phase shift of 0.0030 m between the upper and lower stators was introduced. In addition, according to the result in Fig. 14(b), the minimized cogging force can be achieved when the stator tooth width is 0.0084 m, but the tooth width of 0.0076 m was used in order to secure a sufficient coil volume. Fig. 15(a) and (b) shows the nonslot-phase- and slot-phase-shift configurations with the same stators, respectively.

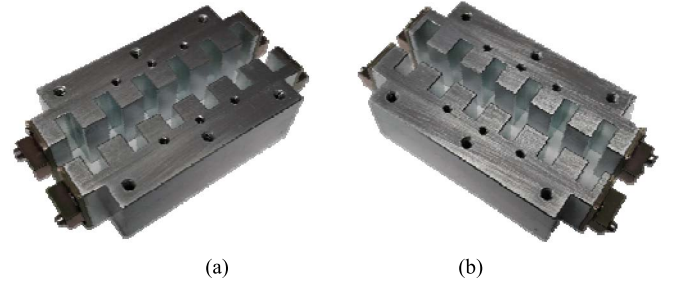


Fig. 15. Comparison of two different arrangements for double-sided stators. (a) Nonslot-phase-shift configuration. (b) Slot-phase-shift configuration.

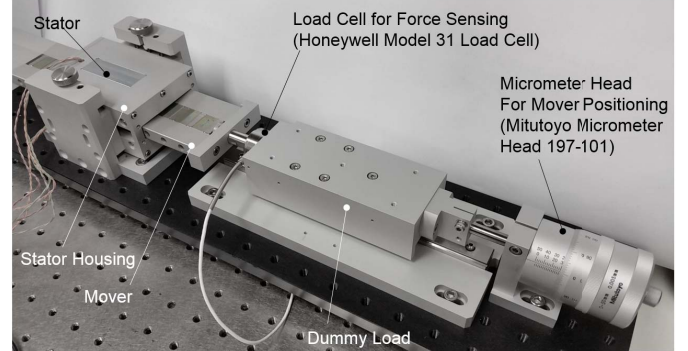


Fig. 16. Photograph of the experimental setup to measure the total detent- and steady-state thrust forces.

IV. TOTAL DETENT- AND STEADY-STATE THRUST FORCE MEASUREMENTS

The experimental setup to measure the total detent- and steady-state thrust forces according to the mover positions is shown in Fig. 16. The copper wire of 26 AWG is used for the phase coils with the number of turns of 85 for each coil. The same phase coils in the upper and lower stators are connected in series in order to apply the phase currents.

Fig. 17 shows the comparison of the predicted thrust forces of the infinite-length model and the measured thrust forces of the prototype configured with the step-shaped end frames and without slot-phase-shift, as shown in Fig. 15(a). The steady-state thrust forces were evaluated according to the mover positions in the case that the currents of -5 A (-425 A-turns), 10 A (850 A-turns), and -5 A (-425 A-turns) are supplied to phases a , b , and c , respectively. The FEA results estimated a slightly smaller force than the real measurements. This seems to be due to the fact that the practical permeability of the physical material was higher than the simulation value. The total detent force was also measured under the condition that all phase currents are set to be zero. It is apparent that the total cogging force becomes the dominant detent force due to the significant reduction of the end-effect force. This result also validates the proposed techniques using the separate optimal approaches for the cogging and end-effect forces. In addition, although the measured detent force was reduced to be 23% of that of the base model as compared with the results given in Fig. 2, the thrust force is still distorted by the third-harmonic cogging force.

The results in Fig. 18 also show the thrust-force comparisons of the slot-phase-shifted infinite-length model and the

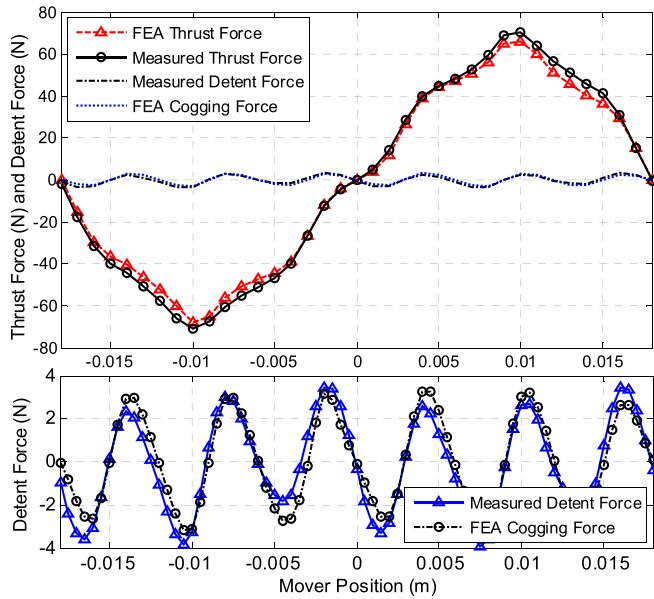


Fig. 17. Comparison of the predicted and measured thrust forces (top), and comparison of the predicted cogging and measured detent forces (bottom) when $T_t = 0.0076$ m.

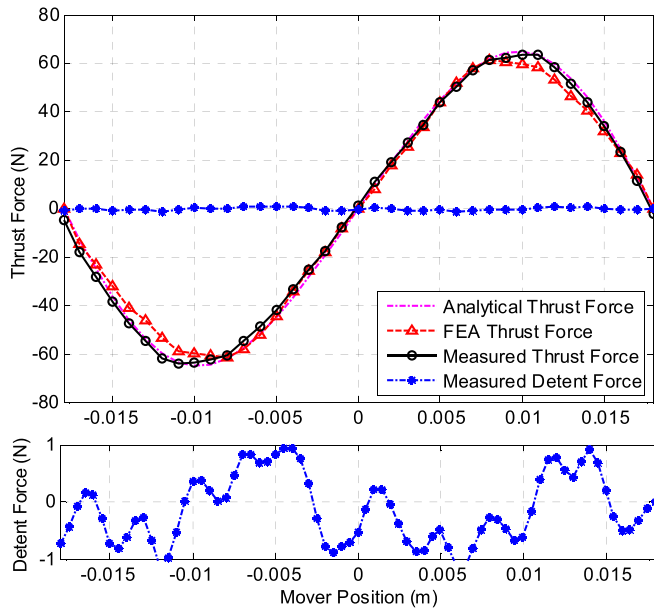


Fig. 18. Maximum thrust force and detent force comparison (top), and magnified view of the detent force from the top figure (bottom).

prototype shown in Fig. 15(b). The same current conditions were applied. The thrust force was also calculated by the analytic force equation. The analytic solution for the thrust force is in good agreement with the measurement, but the FEA result is estimated as a slightly smaller force than the real measurement like the above FEA result. The measured detent force was reduced to be 6% of that of the base model through the proposed detent-force-free techniques. Its value was approximately 1.5% of the maximum thrust force ($\cong 63.5$ N). In other words, the thrust force corresponding to the mover positions can be generated with no significant force

distortion due to the minimization of the detent forces. This implies that high-precision motion control of the double-sided 6/4 IPM-FLBM can be achieved with a proper controller.

V. CONCLUSION

New practical detent-force minimization methodologies for the double-sided 6/4 IPM-FLBM were presented in this paper. The end-effect force was remarkably reduced through the 2-D optimization using the step-shaped end frames. The solutions to the 1-D and 2-D optimizations were formulated with measuring the end-effect force of one side of the slotless stator, and their validity was demonstrated experimentally. In addition, the slot-phase-shift technique based on the cogging-force model with the infinite-length stator was newly implemented to minimize the cogging force. The optimal slot-phase shift between the upper and lower stators was formulated by an analytic expression for practical applications. The validity of this optimal solution was verified with actual measurements. Eventually, a detent-force-free double-sided IPM-FLBM with the detent force of only 1.5% of the maximum thrust force was designed and constructed after a 94% reduction of the detent force. The advantage of the proposed techniques is that there are no excessive size changes, fabrication difficulties, or additional parts as compared with the conventional approaches.

REFERENCES

- [1] J. F. Gieras, Z. J. Piech, and B. Z. Tomczuk, "Topologies and selection," in *Linear Synchronous Motors*, 2nd ed. Boca Raton, FL, USA: CRC Press, 2012, pp. 1–22.
- [2] I.-S. Jung, J. Hur, and D.-S. Hyun, "Performance analysis of skewed PM linear synchronous motor according to various design parameters," *IEEE Trans. Magn.*, vol. 37, no. 5, pp. 3653–3657, Sep. 2001.
- [3] Y.-W. Zhu, D.-H. Koo, and Y.-H. Cho, "Detent force minimization of permanent magnet linear synchronous motor by means of two different methods," *IEEE Trans. Magn.*, vol. 44, no. 11, pp. 4345–4348, Nov. 2008.
- [4] C.-C. Hwang, P.-L. Li, and C.-T. Liu, "Optimal design of permanent magnet synchronous motor with low cogging force," *IEEE Trans. Magn.*, vol. 48, no. 2, pp. 1039–1042, Feb. 2012.
- [5] M. Inoue and K. Sato, "An approach to a suitable stator length for minimizing the detent force of permanent magnet linear synchronous motors," *IEEE Trans. Magn.*, vol. 36, no. 4, pp. 1890–1893, Jul. 2000.
- [6] S. W. Youn, J. J. Lee, H. S. Yoon, and C. S. Koh, "A new cogging-free permanent-magnet linear motor," *IEEE Trans. Magn.*, vol. 44, no. 7, pp. 1785–1790, Jul. 2008.
- [7] N. Bianchi, S. Bolognani, and A. D. F. Cappello, "Reduction of cogging force in PM linear motors by pole-shifting," *IEE Proc.-Electr. Power Appl.*, vol. 152, no. 3, pp. 703–709, May 2005.
- [8] K.-C. Lim, J.-K. Woo, G.-H. Kang, J.-P. Hong, and G.-T. Kim, "Detent force minimization techniques in permanent magnet linear synchronous motors," *IEEE Trans. Magn.*, vol. 38, no. 2, pp. 1157–1160, Mar. 2002.
- [9] S.-G. Lee, S.-A. Kim, S. Saha, Y.-W. Zhu, and Y.-H. Cho, "Optimal structure design for minimizing detent force of PMLSM for a ropeless elevator," *IEEE Trans. Magn.*, vol. 50, no. 1, Jan. 2014, Art. ID 4001104.
- [10] D. Ishak, Z. Q. Zhu, and D. Howe, "Comparison of PM brushless motors, having either all teeth or alternate teeth wound," *IEEE Trans. Energy Convers.*, vol. 21, no. 1, pp. 95–103, Mar. 2006.
- [11] A. M. El-Refaie, T. M. Jahns, and D. W. Novotny, "Analysis of surface permanent magnet machines with fractional-slot concentrated windings," *IEEE Trans. Energy Convers.*, vol. 21, no. 1, pp. 34–43, Mar. 2006.
- [12] D. W. Novotny and T. A. Lipo, *Vector Control and Dynamics of AC Drives*, 1st ed. New York, NY, USA: Oxford Univ. Press, 1996.
- [13] P. J. Hor, Z. Q. Zhu, D. Howe, and J. Rees-Jones, "Minimization of cogging force in a linear permanent magnet motor," *IEEE Trans. Magn.*, vol. 34, no. 5, pp. 3544–3547, Sep. 1998.
- [14] J. Pyrhönen, T. Jokinen, and V. Hrabovcová, *Design of Rotating Electrical Machines*, 1st ed. New York, NY, USA: Wiley, 2008.

Young-Shin Kwon (S'11) received the B.S. degree in control and instrumentation engineering from Hanyang University, Seoul, Korea, in 1995, and the M.S. degree in control and instrumentation engineering from Seoul National University, Seoul, in 1997. He is currently pursuing the Ph.D. degree with the Department of Mechanical Engineering, Texas A&M University, College Station, TX, USA.

He was the Automatic Transmission System Developer with Hyundai Electronics Corporation, Icheon, Korea, for two years, after the M.S. degree. He also developed the active seekers of guided missile systems and naval/airborne radar systems as a Principal Researcher with LIG Nex1 Corporation, Yongin, Korea, for 13 years. His current research interests include design and analysis of spatial stabilization of multi-axis platforms, opto-mechatronics systems, and linear magnetic actuators.

Won-jong Kim (S'89–M'97–SM'03) received the B.S. (*summa cum laude*) and M.S. degrees in control and instrumentation engineering from Seoul National University, Seoul, Korea, in 1989 and 1991, respectively, and the Ph.D. degree in electrical engineering and computer science from the Massachusetts Institute of Technology, Cambridge, MA, USA, in 1997.

He has been with the Department of Mechanical Engineering, Texas A&M University, College Station, TX, USA, since 2000, where he is currently an Associate Professor and was the Inaugural Holder of the Dietz Career Development Professorship II from 2007 to 2010. He holds three U.S. patents in precision positioning systems. His current research interests include the analysis, design, and real-time control of mechatronic systems, networked control systems, and nanoscale engineering and technology.

Prof. Kim is a fellow of the American Society of Mechanical Engineers (ASME) and a member of Pi Tau Sigma. He is or was a Technical Editor of the IEEE/ASME TRANSACTIONS ON MECHATRONICS, the ASME *Journal of Dynamic Systems, Measurement and Control*, the *International Journal of Control, Automation, and Systems*, and the *Asian Journal of Control*.